J. Cent. South Univ. (2026) 33: 484−505
DOI: https://doi.org/10.1007/s11771-026-6156-y

Springer

Research Article

A novel passive flow control method employing vortex generators to suppress wake flow characteristics of a high-speed train: Mechanism and application

HAN Shuai(韩帅)[1, 2, 3, 4], ZHANG Jie(张洁)[1, 2, 3]*, TUDBALL-SMITH Daniel[4], BURTON David[4], THOMPSON Mark[4]

1. State Key Laboratory of Heavy-duty and Express High-power Electric Locomotive, Central South University, Changsha 410075, China;
2. Key Laboratory of Traffic Safety on Track of Ministry of Education, School of Traffic & Transportation Engineering, Central South University, Changsha 410075, China;
3. National & Local Joint Engineering Research Center of Safety Technology for Rail Vehicle, Central South University, Changsha 410075, China;
4. Fluids Laboratory for Aeronautical and Industrial Research (FLAIR), Department of Mechanical and Aerospace Engineering, Monash University, Clayton, VIC 3800, Australia

© Central South University 2026

Abstract: This paper proposes a passive control method to reduce peak values of slipstream and turbulent kinetic energy in a high-speed train wake by attaching vortex generators (VGs) onto the upper surface of the tail car. The impact of the VGs is assessed through the improved delayed detached eddy simulations (IDDES) after validating predictions against previous experimental measurements and other numerical predictions for the base case. The simulations indicate that strategically installed VGs can reduce the average slipstream velocity ($U_{\text{slipstream}}$) and the upper limit of slipstream velocity ($U_{\text{slipstream, max}}$) by ~17% and ~15%, respectively, as well as moving the peaks downstream by approximately train height, thus reducing the danger posed by slipstream to waiting passengers and trackside workers. Analysis shows that the wake turbulent kinetic energy diminishes as the vortex generators decelerate the downwash flow and reduce shear production in the wake. It is also found that the presence of VGs significantly impacts the flow on the upper surface near the tail by modifying the unsteady trailing longitudinal vortices through the formation of additional counter-rotating longitudinal vortices from the VGs. These latter vortices prevent the merging of vortical airflow around the trailing nose tip, which is otherwise induced by the longitudinal vortex of the train. They also reduce vortex intensity through cross-annihilation and cross diffusion as the wake advects downstream, limiting outwards advection through interaction with the image pair, and contributing to a decrease in the peak slipstream value. The method proposed offers a simple approach to wake control leading to significant slipstream benefits.

Keywords: high-speed train; vortex generators; slipstream; wakes; passive control

Cite this article as: HAN Shuai, ZHANG Jie, TUDBALL-SMITH Daniel, BURTON David, THOMPSON Mark. A novel passive flow control method employing vortex generators to suppress wake flow characteristics of a high-speed train: Mechanism and application [J]. Journal of Central South University, 2026, 33(1): 484−505. DOI: https://doi.org/10.1007/s11771-026-6156-y.

Foundation item: Project(52372370) supported by the National Natural Science Foundation of China; Project(2023ZZTS0379) supported by the Graduate Student Independent Innovation Project of Central South University, China; Project(202206370058) supported by the China Scholarship Council

Received date: 2025-05-06; **Accepted date:** 2025-10-11

Corresponding author: ZHANG Jie, PhD, Professor; E-mail: j.zhang@csu.edu.cn; ORCID: https://orcid.org/0000-0003-3831-2993

1 Introduction

With continuing advances in science and technology, the potential maximum speeds of high-speed trains continue to increase. However, with a rise in potential speed, train aerodynamics becomes increasingly important, including increased aerodynamic forces and accentuated slipstream disturbances [1 − 3]. These issues represent substantial challenges to the efficient and safe operation of high-speed trains.

The induced wake of a train is an important factor that affects aerodynamic performance, particularly by influencing the velocity of the slipstream [4 − 6]. The slipstream velocity is the induced air velocity as the train passes through a stationary/near-stationary atmosphere. The slipstream is influenced by multiple factors, primarily the train's operating speed and geometric configuration. With the rapid development of high-speed trains, slipstream effects have raised important safety concerns, including potential hazards to platform passengers and damage to trackside infrastructure. Running at high speeds, the movement of the train through the atmosphere significantly perturbs the surrounding air, inducing an unsteady turbulent wake flow that is effectively dragged by the train [7 − 9]. The wake is composed of shear layers, shed vortices, separation and reattachment regions, and a pair of time-mean counter-rotating longitudinal or streamwise vortices. These vortices are caused by the interaction between the downwash flow over the roof and tail and merging flow from the sides. Due to mutual induction and interaction with the ground, as they move further downstream of the train tail, these vortices continue to move downwards and outwards, exacerbating the three-dimensional, complex, and unsteady flow characteristics of the train wake [10 − 13]. When the train is running, the wake develops continuously, and the vortices shed alternately, increasing the pressure difference between the head and tail of the train. The interaction between the downwash flow over the roof and tail and the flow from the sides strongly affects the lift on the tail car, increasing the risk of derailment. The highest slipstream velocity occurs in the wake region of the train [12 − 14]. Methods that influence the structure of the wake can be beneficial for improving the aerodynamic performance of a train, and reducing the danger posed by slipstream to waiting passengers and trackside workers.

Vortex generators (VGs) are effective in realizing flow control and have been extensively used in aircraft, cars, and other applications [15 − 19]. With simple compact structures, vortex generators are easy to apply in engineering applications, and no additional energy input is needed to influence the passing flow. Conventional vortex generators applied on aircraft have been used mainly to control boundary layer flows, with their size comparable to the boundary layer thickness. The use of vortex generators can delay flow separation from the wings and provide a measurable reduction in drag [15, 17, 20]. In contrast, the focus of vortex generators used in automotive racing is to reduce pressure along the tail by creating stable and strong vortices [16]. With heights higher than the thickness of the boundary layer, vortex generators can produce a suction force between the vehicle and the ground, improving cornering traction [21]. As these applications indicated, vortex generators play a significant role in improving aerodynamic performance. Nevertheless, the existing experience with vortex generator applications in conventional road vehicles cannot be directly applied to high-speed trains due to their more streamlined shapes with no fixed flow separation points [22].

Some researchers have conducted preliminary investigations into the application of vortex generators to high-speed trains focusing primarily on reducing aerodynamic drag, with some examples shown in Figure 1. KRAJNOVIĆ [23] optimized the placement of vortex generators for the purpose of drag reduction, while LI et al [24] found that the length of the streamlined nose (tail car) has a significant influence on the drag reduction effect of the VGs. These findings suggest that the impact of VGs on trains with highly streamlined designs requires further investigation [25]. In previous studies, VGs were strategically placed around the streamlined transition position, aiming to proactively induce controlled flow separation and thereby effectively attenuate the primary separation vortex. However, for streamlined high-speed trains,

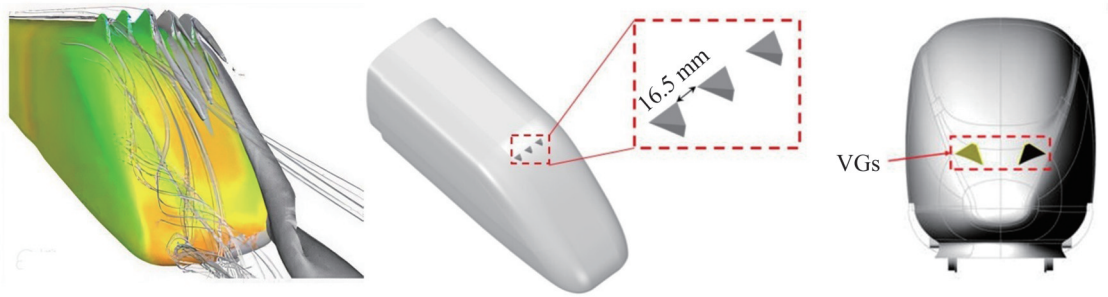


Figure 1 The placement of VGs on different high-speed trains [23−25]

changes to the slipstream induced by vortex generators are still unclear. This paper aims to explore the effect of vortex generators on wake formation, and how these changes impact turbulent kinetic energy and slipstream velocity in the wake. Exploring these influences is of considerable importance to improving the aerodynamic performance of high-speed trains.

This paper employs the improved delayed detached eddy simulations (IDDES) to investigate the effect of vortex generators on an HST wake. Comparisons against wind-tunnel tests and moving-model tests demonstrate the fidelity of the numerical modelling. The effects of vortex generators placed at two different positions are analyzed, and the predictions highlight the physical mechanisms leading to slipstream velocity suppression and turbulent kinetic energy reduction. It is observed that VGs decelerate the downwash flow on the upper surface of the high-speed train, increasing the positive pressure on the tail car. Simultaneously, vortex generators feed in additional vorticity of opposite sign reduce the intensity of the trailing longitudinal vortices. The interaction between these two pairs of counter-rotating vortices continues as the wake advects downstream, contributing to the reduction of the turbulent kinetic energy and slipstream velocity. Analysis of these results can be beneficial to understanding wake flow structures and how to manipulate them.

2 Methodology

2.1 Computational model

This study employed a high-speed train model including the bogies and windshields. The model geometry is based on the publicly available ICE3 train model, which is a simplified version of the Deutsche Bahn Inter-city Express used widely across Europe. The model geometry is available through the DIN Standards Railway Committee [26]. The train model consisting of two carriages was aimed at producing a slightly simplified flow that would be more amenable to analysis and interpretation. The height of the train was H= 0.18 m, with the total length L=14.3H, and the width W=0.8H.

Three computational models were set up to investigate the impact of vortex generators on the aerodynamic performance of the train, as shown in Figure 2. Note that the vortex generators are located on the tail car, perpendicularly attached to the train's upper surface. The location of vortex generators is a critical factor influencing their effectiveness in flow control. In this study, two promising positions were identified for their placement on the train model, designated as A and B. VG_A indicates that the VGs were placed at position A, situated 0.13H upstream of the tail tip of the train and at 0.07H distance from the central longitudinal plane. VG_{AB} denotes the simultaneous placement of VGs at both positions A and B. Here, B is located 0.3H from the tail tip and 0.18H from the central longitudinal plane. The vortex generators used in this research are trapezoidal in shape, with a height of 0.1H, an upper base length of 0.05H, and a lower base length of 0.2H, as shown in Figure 3. This design was previously used by ZHANG et al [25] in their investigations into aerodynamic drag. As indicated, preliminary testing using different VG placements indicated that the selected positions showed promise for their effect on the flow, reducing the intensity of counter-rotating longitudinal wake vortices, which strongly affect slipstream [25].

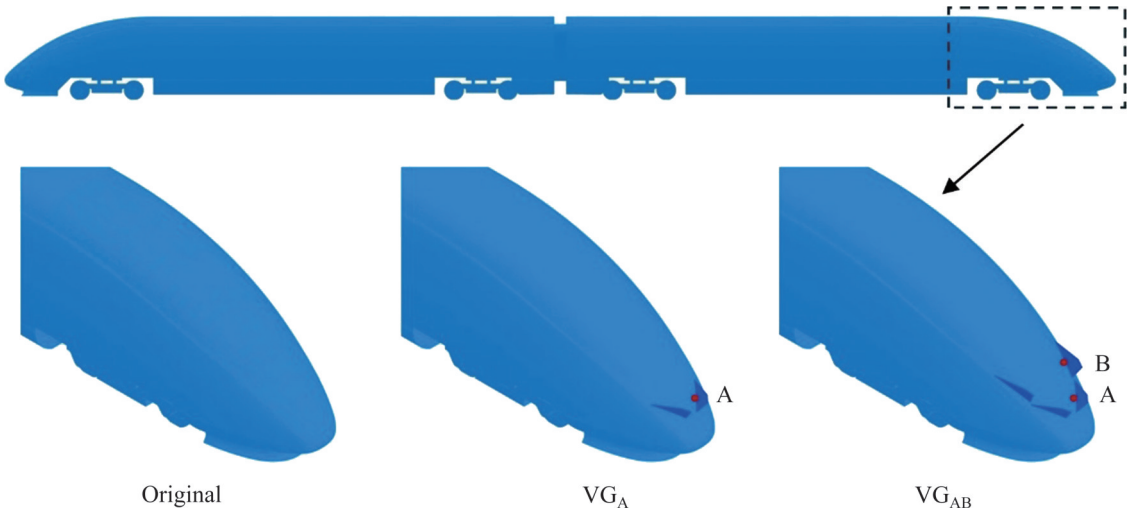


Figure 2 Computational models showing the overall HST model together with views of the tail section showing the placement of the vortex generators

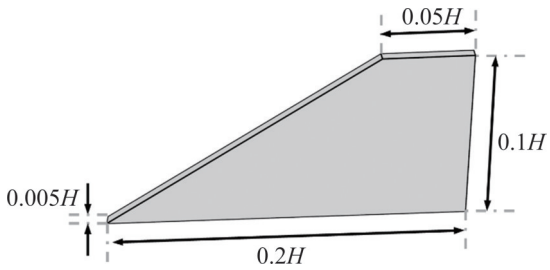


Figure 3 3D design of the vortex generators

2.2 Numerical domain and boundary conditions

The numerical domain is 9H high and 11H wide, as shown in Figure 4. This cross-sectional area leads to a blockage ratio of below 1%. To ensure adequate distance for inflow and downstream wake development, the high-speed train is positioned at a distance of 8H from the entrance of the numerical domain and 30H from the exit [27, 28]. The bottom of the train model is 0.07H from the top of the rails, which, in turn, were set on an elevated track section as used in previous studies [27]. The side walls and upper wall were set as symmetry boundaries. A uniform velocity of U_∞ = 25 m/s was set at the inlet; this gives a Reynolds number of $Re=U_\infty H/\nu$ =3.1×10^5, where ν is the kinematic viscosity. The outlet of the numerical domain was set as a pressure-outlet boundary condition. A no-slip stationary wall boundary condition was applied to the high-speed train surface. The Reynolds number was chosen to maintain consistency with previous wind-tunnel tests [22]. Extensive comparative analyses of slipstream characteristics among wind tunnel tests, moving-model tests, and full-scale measurements at comparable Reynolds numbers have been published in Ref. [29]. Previous research has shown that higher Reynolds numbers promote the formation of small-scale vortices in the train wake while preserving the primary flow structure [30, 31].

2.3 Numerical details

The numerical simulations discussed in this paper were conducted using the commercial flow solver ANSYS Fluent (version 2020 R2). The flow modelling employed the improved delayed detached eddy simulation (IDDES) approach with the shear-stress transport (SST) k-ω wall model. The IDDES model is a hybrid turbulence model blending Reynolds-averaged Navier-Stokes (RANS) near-wall simulation and large eddy simulation (LES), applying RANS to simulate the boundary layer and using LES to capture the large-scale turbulent flow away from boundaries. This has been widely and successfully adopted for the train aerodynamics [32–34]. The SST k-ω model was chosen for the RANS model within the IDDES model because of its ability to simulate the near-wall boundary layer, in particular, its capability of capturing flow separation in adverse pressure gradients. The IDDES model applies an improved delayed shielding function to obtain accurate predictions within the RANS-LES blending region, noting that the original detached eddy simulation models experienced difficulty with

this. A detailed description of the IDDES model is given by SPALART [35].

The time derivative was discretized using the inbuilt second-order implicit scheme [36 – 38]. The adopted physical time step should ensure the Courant number is less than 1.0 in more than 99% of the computational cells [27, 28, 38], as shown in Figure 5. The physical time step was selected as $0.05T_{ref}$ in this paper, where a reference time scale based on the train height and freestream velocity is given by $T_{ref}=H/U_{\infty}$. The impact of the physical time step on the simulation results is discussed in Ref. [39]. Unsteady statistics are sampled over a duration of $133T_{ref}$. This duration is approximately equivalent to the time required for the fluid to pass through the whole computational domain three times or to pass the length of the train 20 times. This was found to be long enough to obtain good convergence of the flow statistics, which was ascertained by doubling the integration time for the base simulation and examining convergence.

2.4 Grid generation

The Fluent Meshing package was used to generate poly-hexahedral hybrid meshes for the numerical simulations [25, 33]. To accurately resolve the near-wall flow structure, 15 prism layers were attached to the surface of the train, as shown in Figure 6. For investigating mesh independence of the numerical predictions, simulations were conducted on three meshes, referred to as coarse, medium, and fine. The numbers of cells in the meshes were 17 million, 24 million, and 34 million, respectively, with the increased resolution mainly focused on the near wall regions in order to better resolve flow separation and the flow around the vortex generators.

The details of the computational meshes are shown in Table 1. n^+, Δl^+, and Δs^+ are defined by $n^+=nu_\tau/\nu$, $\Delta l^+=\Delta l u_\tau/\nu$, and $\Delta s^+=\Delta s u_\tau/\nu$, where n is the distance from the train surface to the first node in the wall-normal direction; Δl and Δs are the surface cell sizes at the train surface in the streamwise and spanwise directions, respectively; u_τ is the friction velocity; and ν is the kinematic viscosity. The mean value of n^+ was lower than 1.0 in accordance with recommendations for IDDES to adequately capture flow behavior close to the wall. To provide an indication of grid convergence, the aerodynamic lift and drag forces on the tail car from the different grids are illustrated in Figure 7(a). These aerodynamic force coefficients are defined as follows:

$$C_d=\frac{F_d}{0.5\rho U_\infty^2 S} \tag{1}$$

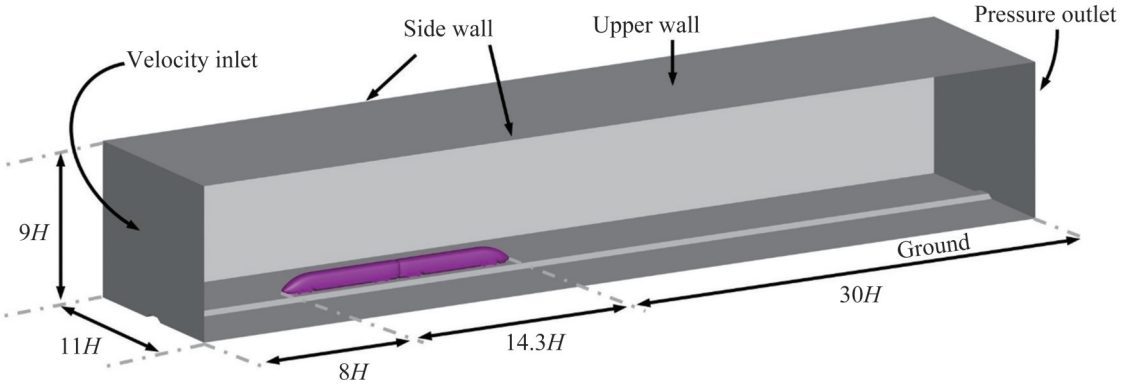


Figure 4 Schematic of the numerical domain showing the positioning of the train relative to domain boundaries

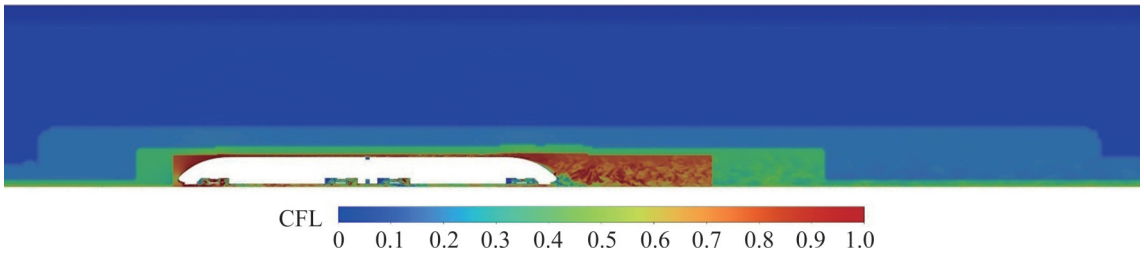


Figure 5 Courant number (CFL) distribution at the middle central plane

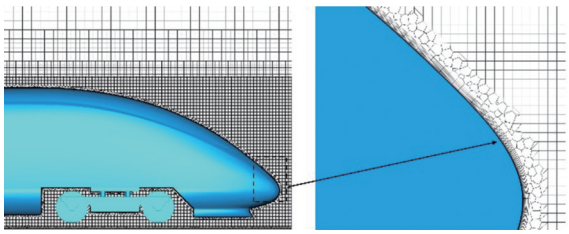


Figure 6 Computational grids

Table 1 Details of the computational meshes indicating wall resolution in the normal (n^+), streamwise (Δl^+) and spanwise (Δs^+) directions in wall units at the train surface

Grid	n^+	Δl^+	Δs^+
Coarse	<1.0	<160	<160
Medium	<1.0	<100	<100
Fine	<1.0	<60	<60

$$C_l = \frac{F_l}{0.5\rho U_\infty^2 S} \tag{2}$$

where F_d and F_l denote the drag and lift forces, respectively; while C_d and C_l represent the corresponding aerodynamic force coefficients. Also, ρ, U_∞, and S signify the air density, the speed of the train, and the cross-sectional area, respectively.

It can be seen that on the fine and medium grids, the predicted drag coefficients show good consistency, while a significantly larger difference is observed for the coarse grid. The iso-surface value Q=1×10^5 s^{-2} was selected for visualization in Figure 7(b) to examine the influence of grid resolution on wake flow structures of the high-speed train model. The results reveal that refined grid resolutions (both medium and fine grids) enable clearer identification of complex flow features around the tail car, consistent with findings in the previous study [40]. Therefore, to balance computational cost and numerical accuracy, the medium grid was used for the study presented here.

2.5 Numerical validation

Moving model tests and stationary ground wind-tunnel tests have been effective ways to examine the aerodynamics of a train. To validate the prediction accuracy of the numerical modelling here, simulation predictions were compared with experimental results from both moving-model tests and stationary-ground wind-tunnel tests [29, 41, 42]. For these validation studies, the same train geometries were used as in the comparison experiments/models but with the same meshing approach and relative resolution as used for the studies reported in this paper.

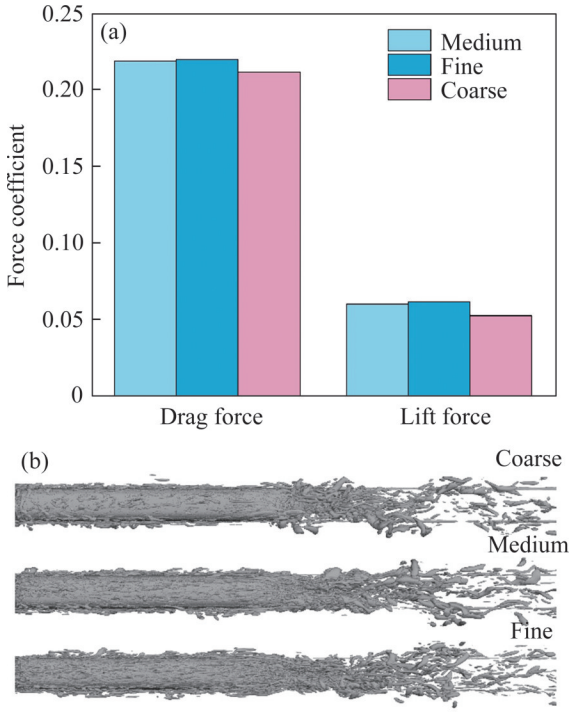


Figure 7 The results obtained from three different grids: (a) The drag and lift coefficients of the tail car; (b) The iso-surfaces of Q-criterion with the value of Q=1×10^5 s^{-2}

Figure 8(a) presents the aerodynamic force coefficients for the tail car obtained from the current simulations, those of XIA et al [42] and those for the stationary wind-tunnel test of BELL et al [29]. There is a strong match between the simulation predictions and those in the referenced articles, with a small difference from the wind-tunnel test. Figure 8(b) shows the time-averaged slipstream velocity obtained by the numerical simulation and moving model test. Although the growth trend of train wake in the numerical simulation differs from that of the moving model test due to variations in ground conditions and slight differences in the geometry of the train [42], the appearance, location and magnitude of the peaks match well. A comprehensive analysis is provided in Ref. [42]. Note that the match is similar to that obtained from IDDES predictions [40, 42]. These data provide reasonable confidence in the reliability of the modeling for aerodynamic force and slipstream

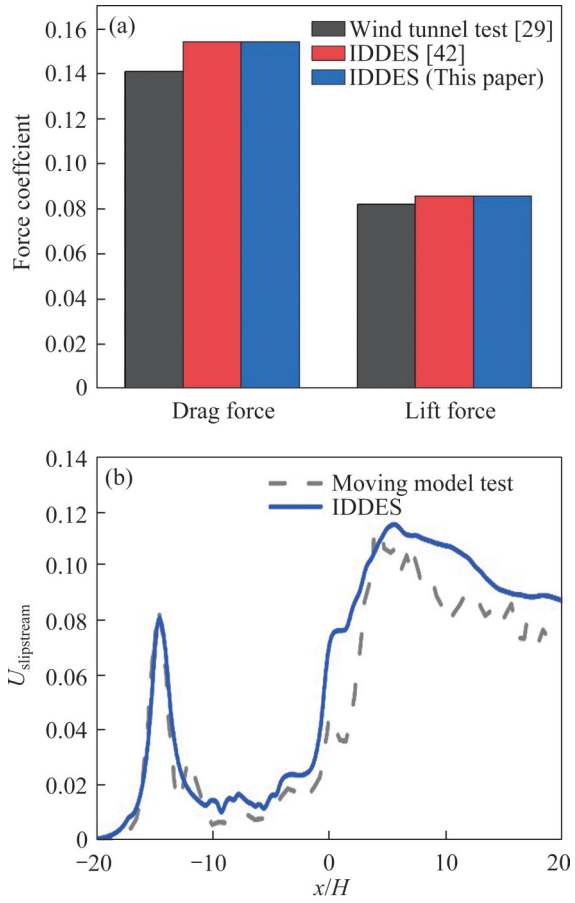


Figure 8 Model validation: (a) The force coefficient comparisons with previous independent IDDES predictions [42], and wind tunnel tests [29]; (b) Slipstream predictions compared with moving model measurements [41]

velocity predictions based on the current methodology.

3 Results and discussion

3.1 Slipstream evaluation

Time-averaged slipstream profiles and gust analysis are presented in this section to quantify the slipstream in the wake region of the high-speed train. The time-averaged flow characteristics are presented by time-averaged slipstream profiles at the locations specified in the technical specifications for interoperability (TSI) [43]. Additionally, gust analysis was conducted using moving probes to artificially replicate the intricate flow caused by the movement of trains observed in full-scale measurements and moving model tests. The maximum slipstream was estimated by adding twice the standard deviation to the mean value of the slipstream velocity under the guidance of the TSI [43]. Further information on these characterisations is provided in the following two subsections.

3.1.1 Time-averaged slipstream profiles

The time-averaged slipstream velocity and its standard deviation are presented in this section, which are measured at both trackside and platform height as defined by the TSI [43]. The heights of the trackside and the platform from the top of the rail are respectively 0.2 m (z=0.05H) and 1.4 m (z=0.35H) at full-scale. The positioning is in accordance with evaluating the effect of the slipstream induced by high-speed trains on both the trackside facilities, and passengers waiting on a platform as a train passes through a station. The time-averaged slipstream velocity profiles cover the longitudinal range from x=−12H to x=28H, set at 3 m away from the train centreline.

Formally, slipstream refers to the airflow movement induced by a running train, observed from a stationary ground-fixed (GF) reference frame. In contrast, a train-fixed (TF) reference frame was adopted in the numerical simulation, indicating that a transition between these two reference frames is necessary for analysis. The normalized streamwise velocity based on the ground-fixed reference frame is given by $U_{GF}=(U_\infty - U_{TF})/U_\infty$, where U_{TF} denotes the streamwise velocity based on the train-fixed reference and U_∞ represents the freestream velocity at the inlet of the domain. The expression for transverse velocity remains consistent across different reference frames, and the normalized transverse velocity based on a ground-fixed reference frame is defined by $V_{GF}=V_{TF}/U_\infty$. The slipstream velocity is defined in accordance with guidelines of the TSI [43] as follows:

$$U_{slipstream}=\sqrt{U_{GF}^2+V_{GF}^2} \tag{3}$$

Note that it does not include the vertical velocity component. The nominal maximum slipstream velocity is defined by $U_{slipstream,max}=U_{slipstream}+2\sigma_{slipstream}$, which estimates the upper limit of slipstream velocity at a 95% confidence level, under the assumption that the samples follow a normal distribution.

Figure 9 depicts the time-averaged slipstream velocity, the streamwise and transverse velocity components, alongside their respective standard

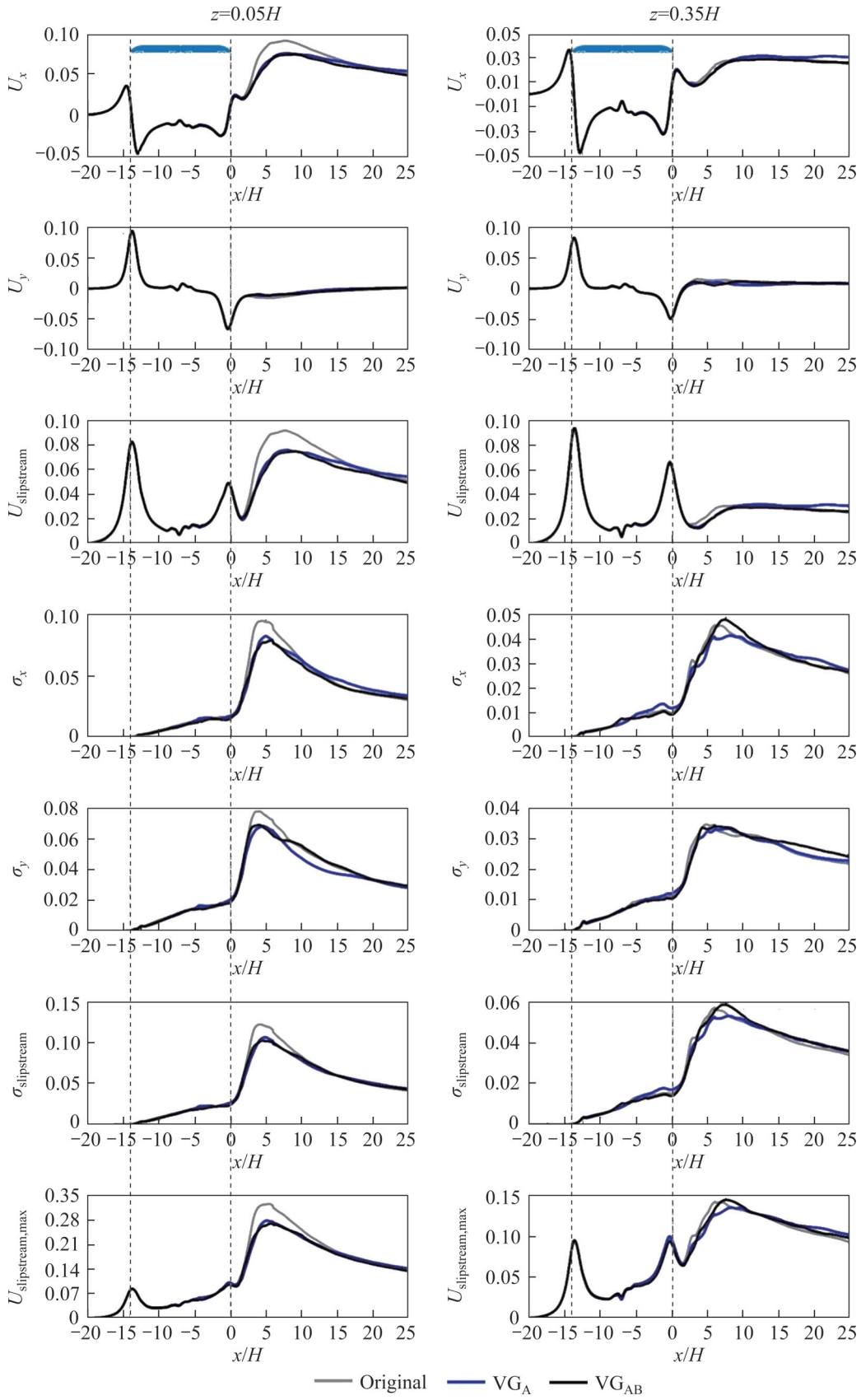


Figure 9 The comparison of the time-averaged slipstream profiles of the two vortex generator configurations with the base case (The rows show longitudinal slipstream velocity (U_x), cross-stream velocity (U_y), slipstream velocity ($U_{\text{slipstream}}$), longitudinal, cross-stream and total standard deviation (σ_x, σ_y and $\sigma_{\text{slipstream}}$) and projected maximum slipstream ($U_{\text{slipstream,max}}=U_{\text{slipstream}}+2\sigma_{\text{slipstream}}$))

deviations at the standard trackside and platform heights. In general, vortex generators have a more significant impact on the trackside slipstream than the slipstream at the platform height. The primary difference in $U_{\text{slipstream}}$ among the three cases predominantly arises from the altered streamwise velocity. However, the VGs noticeably reduce the peak value of standard deviation.

To quantitatively analyze the effect of the VGs on the trackside slipstream, critical values are presented in Table 2 demonstrating that the peak values of $U_{\text{slipstream}}$ and $\sigma_{\text{slipstream}}$ are diminished and delayed to further downstream with VGs. Compared with the original case, VG_A leads to a 17.4% reduction in the peak value of $U_{\text{slipstream}}$, coupled with a 0.35H delay of the downstream peak. In addition, VG_A significantly decreases the peak value of $\sigma_{\text{slipstream}}$ by 13.0% and delays the location of the peak by 0.74H. With a substantial reduction of the mean and standard deviation, the peak value of $U_{\text{slipstream,max}}$ was diminished by 14.6%. With an additional pair of vortex generators at position B, the peak value of the slipstream velocity was further diminished. VG_AB leads to an 18.5% reduction in the peak value of $U_{\text{slipstream}}$, coupled with a 1.41H delay of the downstream peak. The peak values of $\sigma_{\text{slipstream}}$ and $U_{\text{slipstream,max}}$ are diminished by 16.3% and 16.8%, respectively, compared to the original case.

3.1.2 Gust analysis

An alternative way to quantify slipstream is to use gust analysis, which mimics the approach used in moving model experiments. It is consistent with undertaking velocity measurements as a train passes a fixed position. Gust analysis in this section was conducted using 20 moving probes under the TSI specification [43]. The 20 moving probes were placed at z=0.2 m on a plane 3 m away from the middle vertical plane of a full-scale high-speed train to measure the flow at the trackside height. The spacing of the moving probes was equivalent to 20 m at full scale, allowing for independent velocity measurements. The slipstream velocity data were captured by each moving probe and a 1 s moving-average (1 s MA) filter was applied to the raw data.

Figure 10 displays the instantaneous slipstream velocities at trackside height, in which the slipstream velocity values measured by the 20 moving probes are plotted as gray solid curves, while blue solid curves represent the data subject to a 1 s MA filter. The peak values of individual measurements are depicted as black and blue dot points, respectively. Figure 10 clearly demonstrates that the vortex generators effectively decrease the occurrence of high peak values (e. g., greater than 0.4) in the train slipstream.

For a quantitative analysis of the impact of the vortex generators, the mean value $\overline{U}$, and standard deviation σ of the peak values are calculated and shown in Table 3. The final maximum slipstream velocity was defined as $U_{2\sigma}=\overline{U}+2\sigma$ under the TSI specification [43]. In the gust analysis, VG_A and VG_AB exhibit similar effects, primarily influencing the peak value of $U_{2\sigma}$ by altering the standard deviations. Compared with the original case, VG_AB induced a 26.2% reduction in the peak value of σ and a 21.0% decrease in the peak value of $U_{2\sigma}$ in the absence of a 1 s MA. With the application of a 1 s MA, the peak values of σ and $U_{2\sigma}$ are decreased by 19.2% and 15.1%, respectively.

3.2 Turbulent kinetic energy budgets

An examination of the wake turbulent kinetic energy (TKE) is the focus of this section in order to understand the effect of the vortex generators on the dynamics of turbulence generation and transport. The total turbulent kinetic energy is defined as $k=1/2(\overline{u'u'}+\overline{v'v'}+\overline{w'w'})$, where $\overline{u'u'}$, $\overline{v'v'}$, and $\overline{w'w'}$ are the normal Reynolds stresses normalized by the square of the freestream velocity U_∞^2, respectively. The left column of Figure 11 displays the difference in the total turbulent kinetic energy induced by vortex generators in the middle longitudinal plane (y=0).

Table 2 Critical values for the time-averaged trackside slipstream comparison

Case	$U_{\text{slipstream}}$		$\sigma_{\text{slipstream}}$		$U_{\text{slipstream,max}}$	
	Maximum	Location (x/H)	Maximum	Location (x/H)	Maximum	Location (x/H)
Original	0.092	7.64	0.123	4.14	0.328	5.37
VG_A	0.076	7.99	0.107	4.88	0.280	5.09
VG_AB	0.075	9.05	0.103	4.45	0.273	5.90

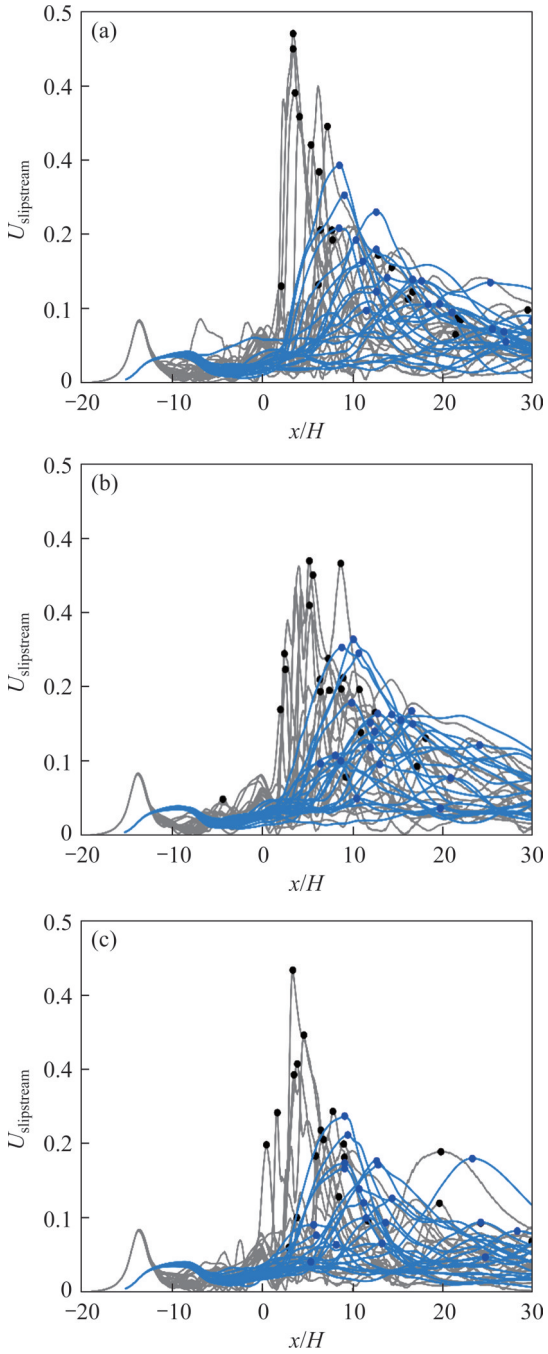


Figure 10 The gust analysis based on the measurements from the artificial moving probe technique under the TSI specification [43] for different cases: (a) Original; (b) VG_A; (c) VG_{AB}. The gray and blue curves denote the raw and 1 s MA filtered slipstream velocities, respectively, with their peaks marked by black and blue dots

The area characterized by values exceeding 0.04 in the wake region experienced a significant reduction with vortex generators. In addition, the distribution of TKE on the y=0.1H plane is depicted in the right column of Figure 11 to illustrate the influence of the vortex generators themselves. Without vortex

Table 3 The unsteady statistics of the gust analysis with and without the 1 s MA

Case	Without 1s MA			With 1s MA		
	$\overline{U}$	σ	$U_{2\sigma}$	$\overline{U}$	σ	$U_{2\sigma}$
Original	0.127	0.149	0.404	0.107	0.078	0.259
VG_A	0.123	0.117	0.356	0.116	0.070	0.253
VG_{AB}	0.106	0.110	0.319	0.094	0.063	0.220

generators, there is an area below the nose tip possessing the highest value within the interval $0 \le x \le 0.6H$. Similarly to the middle vertical plane, vortex generators lead to an obvious decline of the turbulent kinetic energy within this area. However, the presence of the vortex generators placed at position A gives rise to a localized area behind them exhibiting an elevated TKE. The interesting point is that installing a pair of vortex generators at position B significantly reduces the size of this high value region, noticeably diminishing the overall turbulent kinetic energy. The reduction in TKE indicates a decrease in velocity fluctuations within the wake, which is consistent with the observed reduction in the slipstream standard deviation. The normalized shear Reynolds stress $\overline{u'v'}$ on the plane at z=0.05H is displayed in Figure 12 to show the correlation between the streamwise and the spanwise velocity components. With vortex generators, the Reynolds stress $\overline{u'v'}$ becomes weaker in the wake, and the location of the region with high values is delayed by 0.4H. This delay is attributed to changes in the flow structures below the nose tip of the train, which are analyzed in the following section.

To further examine the cause of the reduction of the turbulent kinetic energy, the shear production, which is considered a principal source of TKE, is shown in Figures 13 and 14. This accounts for the production of TKE from mean flow shear. Due to the streamwise velocity being much larger than the other two velocity components [44, 45], the two main components of shear production are given by:

$$P_{suv} = -\overline{u'v'}\left(\frac{\partial U}{\partial y} + \frac{\partial V}{\partial x}\right) \tag{4}$$

$$P_{suw} = -\overline{u'w'}\left(\frac{\partial U}{\partial z} + \frac{\partial W}{\partial x}\right) \tag{5}$$

The shear production, P_{suw}, on the planes at y=0 and y=0.1H, is depicted in Figure 13. On the middle longitudinal plane, a large region with opposite

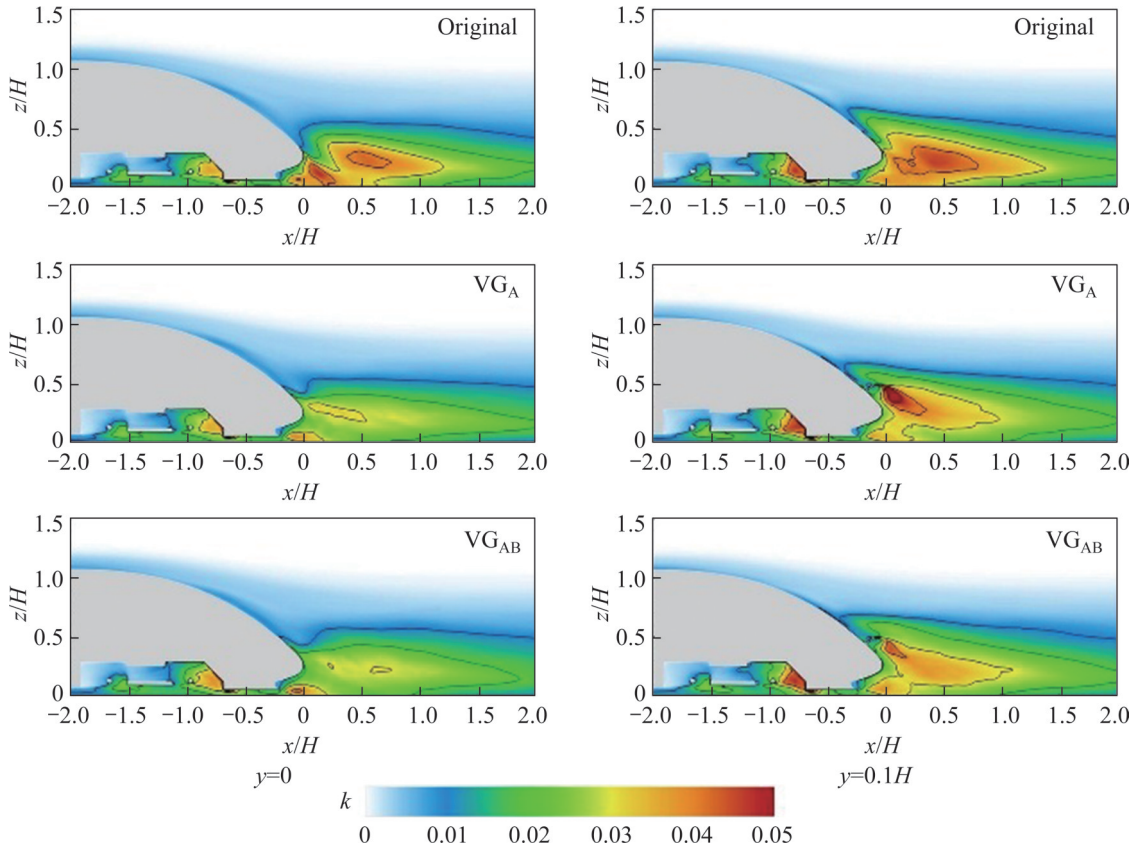


Figure 11 The distribution of TKE projected on the planes at y=0 (centerplane) and y=0.1H (offset from the centerplane)

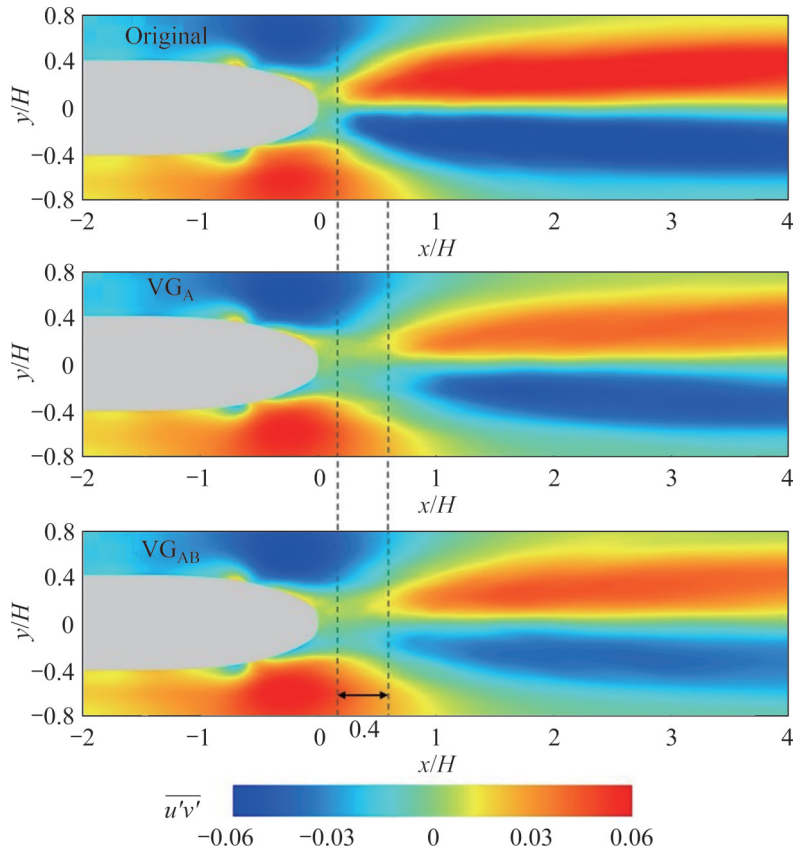


Figure 12 Contours of the Reynolds stress component $\overline{u'v'}$ showing the vortex generators restricting the cross-stream spread of the high-stress regions leading to slipstream reduction

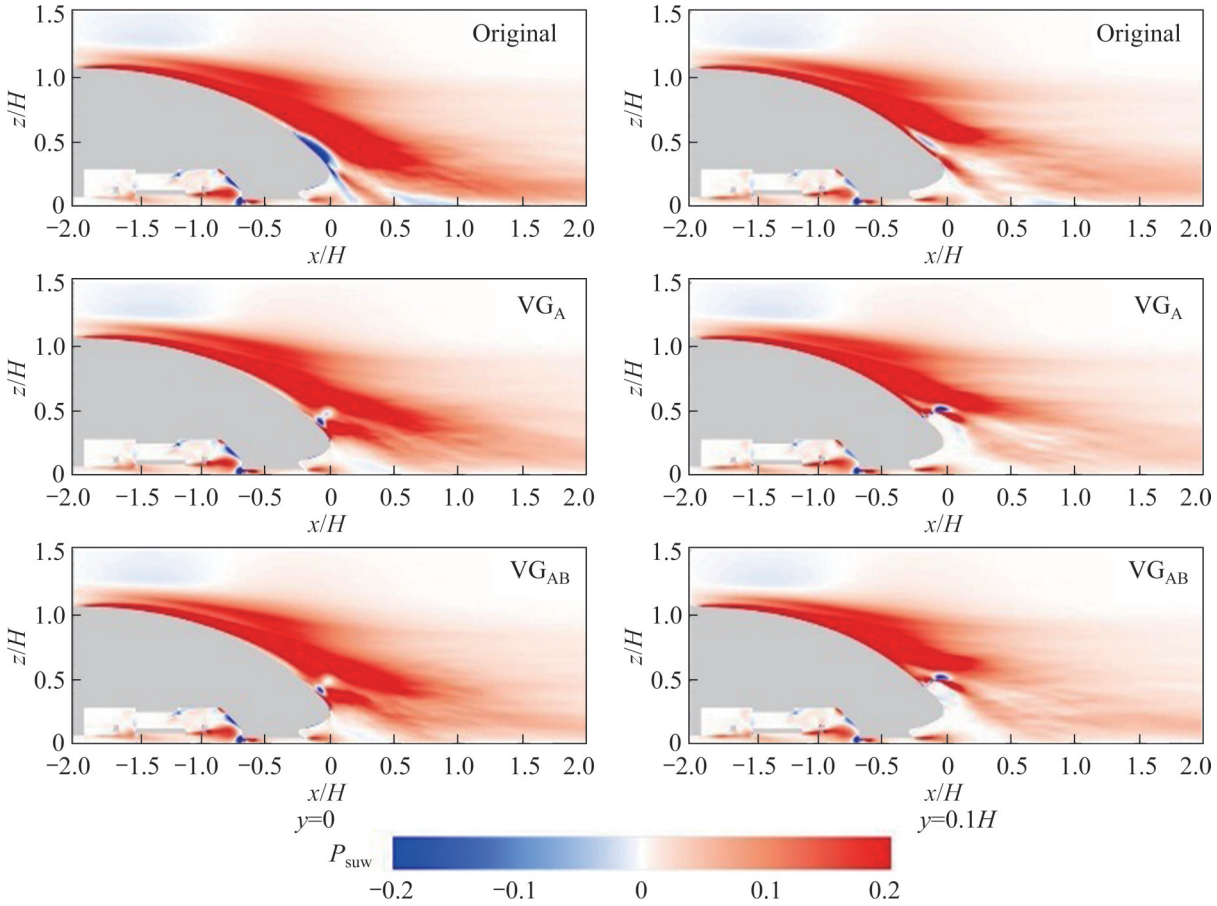


Figure 13 The distribution of shear production P_{suw} in the planes at y=0 and y=0.1H

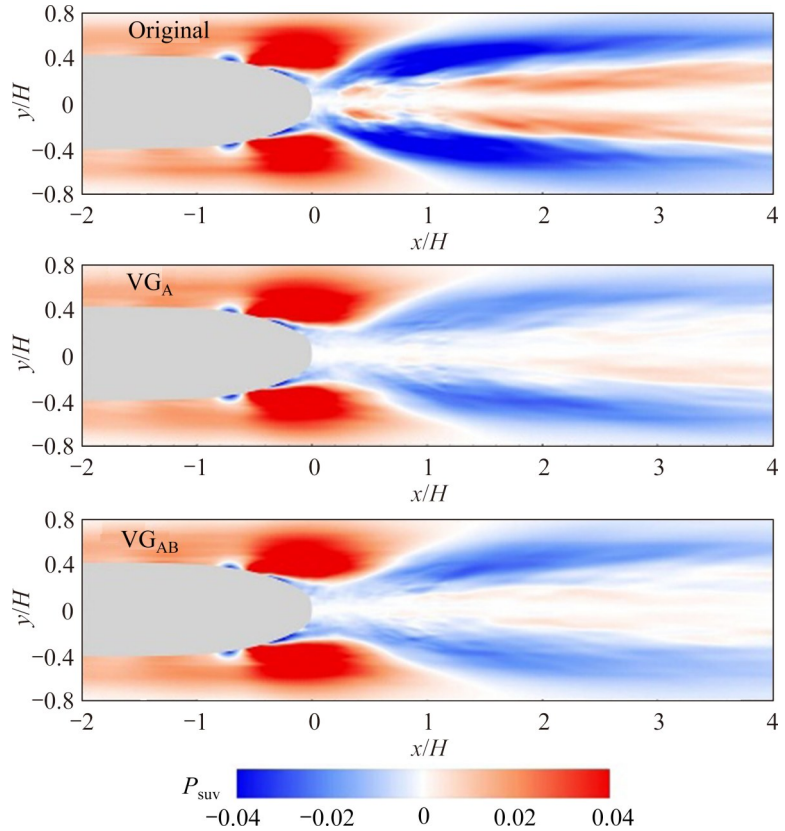


Figure 14 The distribution of shear production P_{suv} in the plane z=0.05H

shear production appears above the upper surface of the train near the nose tip for the original case. However, the VGs disrupt this region by generating and feeding in vorticity resulting in a noticeable decline in extreme values and explaining the reduction in TKE around the nose tip. In addition, the contour of the P_{suw} on the plane at y=0.1H demonstrates that the presence of VGs contributes to a reduction in the shear production around the nose tip. For the further wake region of the train, the shear production P_{suv} on the plane at z=0.05H is depicted in the Figure 14, illustrating the reduction in P_{suv} values due to the influence of VGs. The reduction of shear production suggests decreased turbulence generation and transport, contributing to a more stable wake flow and lower slipstream values.

3.3 Turbulent flow structures

To show the effect of the vortex generators on the flow structures to further understand the reduction of slipstream and turbulent kinetic energy, Figure 15 shows streamlines superimposed on contour maps of the time-averaged spanwise vorticity on the middle longitudinal plane (y=0). Here, the spanwise vorticity is normalized using $\omega_y^+ = \omega_y H/U_\infty$. For all three cases, a recirculation bubble appears due to the flow separation on the upper surface of the train at the location labeled 'a' in the figures. After the recirculation region, the flow again reattaches onto the train surface. A significant difference near the train tail tip is denoted by 'b' in the figures. This illustrates that a adverse pressure gradient occurs for the original case leading to substantial vorticity generation,

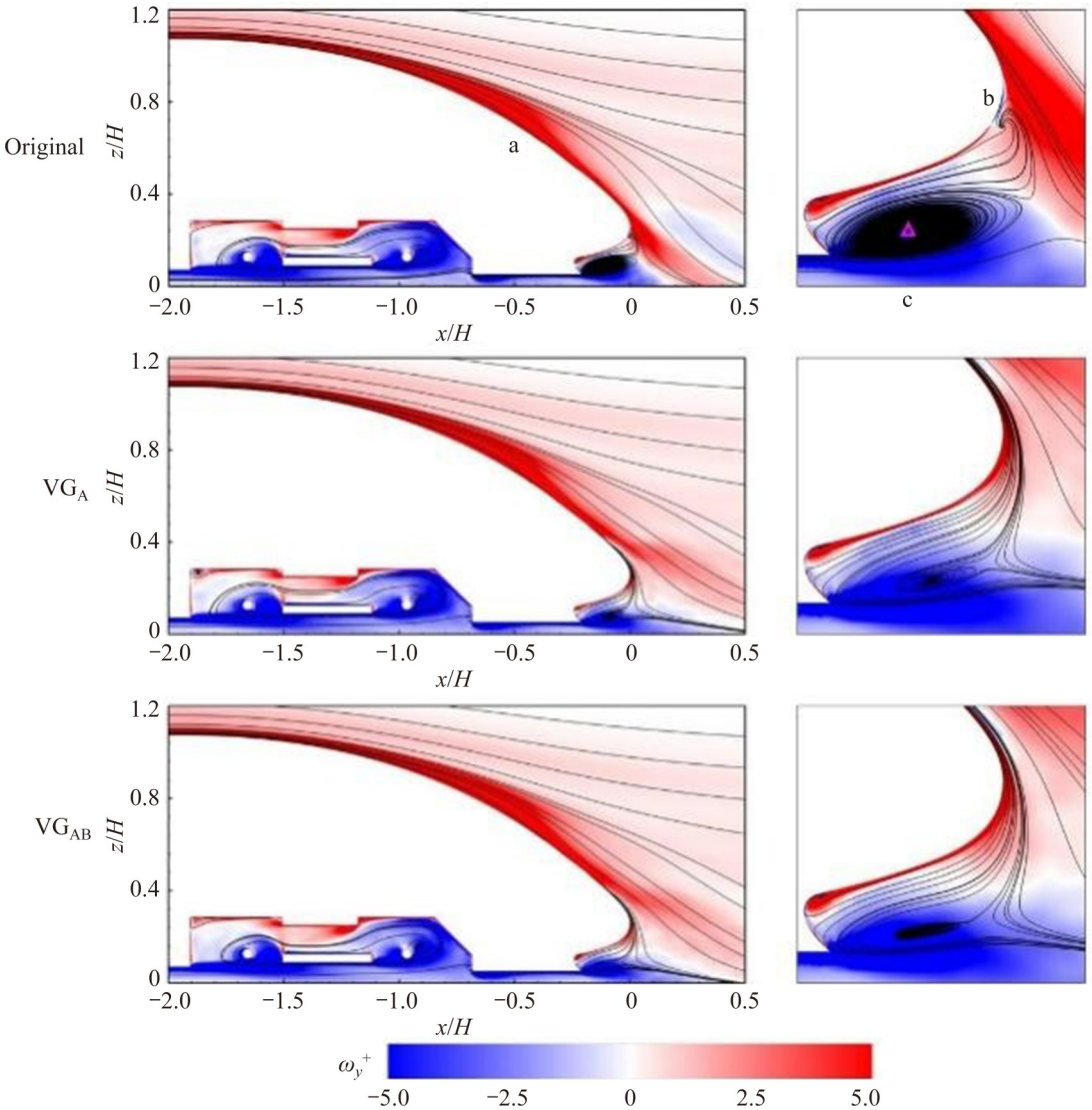


Figure 15 Comparison of streamlines overlaid with the contour maps of the time-averaged spanwise vorticity on the plane y=0

while it disappears due to the delay of flow separation induced by vortex generators. The weak recirculation beneath the nose tip of the train in the original case disappears due to the effect of the VGs, annotated by 'c', which is the primary reason for the delay of the shear Reynolds stress, $\overline{u'v'}$.

A pair of time-mean counter-rotating streamwise vortices plays a pivotal role in the detailed flow contributing to the high-speed train slipstream. Figure 16 displays contour maps of the time-averaged streamwise vorticity on the planes located at x=0.1H, x=1H and x=2H, with the 2D streamlines overlaid on the left and the colored contours of normalized streamwise vorticity on the right. The normalized vorticity was given by $\omega_x^+ = \omega_x H/U_\infty$. The effect of the vortex generators on the near wake is clearly illustrated in the plane x=0.1H, for which the presence of the VGs generates additional opposite-signed vorticity, effectively splitting the streamwise vorticity distribution into two parts. Further downstream, these two parts again merge into slightly more elongated vortices in the vertical direction compared with the original case, as shown on the plane x=1H. Due to mutual induction and interaction with the ground, these vortices move downwards and outwards. On the plane x=2H, the impact of the vortex generators is evident in the reduction in strength of the vortex pair.

Iso-surfaces of time-averaged Q-criterion are depicted in Figure 17 as an intuitive display of the flow structures difference induced by vortex generators. The normalized Q-criterion was given by $Q^* = QH^2/U_\infty^2$, and the iso-surfaces were selected as Q^*=2. The iso-surfaces are colored by ω_x^+ showing the direction of the streamwise vortices. For the original case, a pair of counter-rotating streamwise vortices V_t is generated in the wake region by the interaction of the downwash flow over the roof and the tail with the flow from the sides. These vortices move downwards and outwards as a consequence of mutual induction and interaction with the ground,

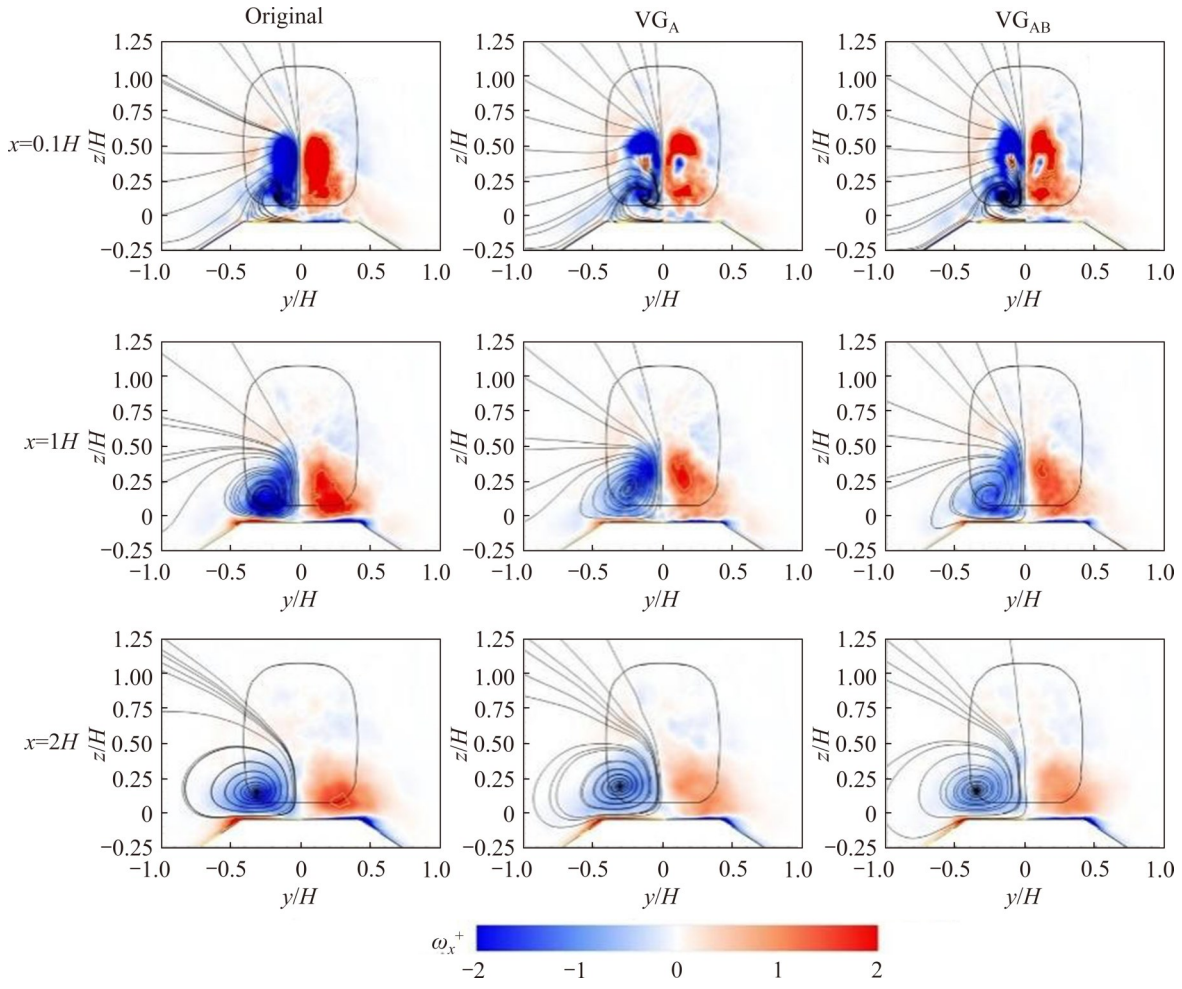


Figure 16 Comparison of the streamwise vortex structures on the planes

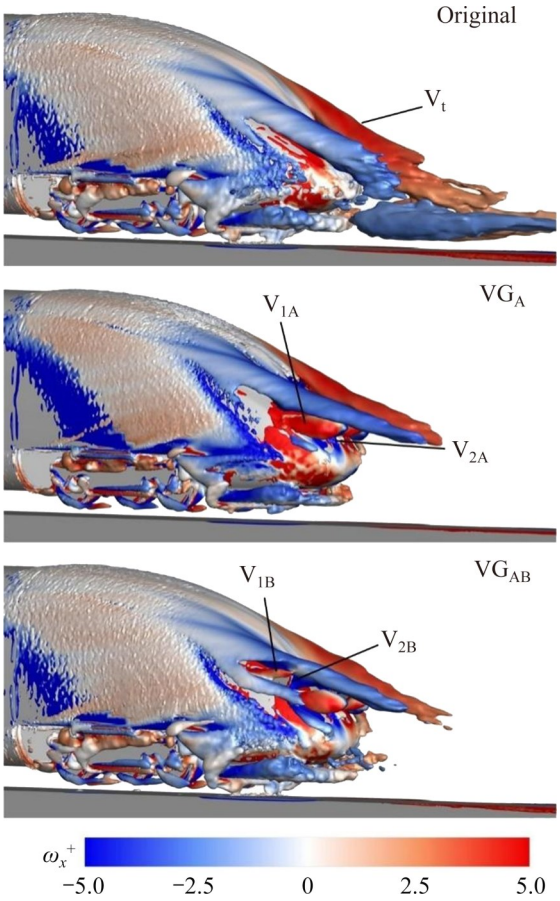


Figure 17 Flow structures visualized by iso-surfaces of Q-criterion at Q^*=2, colored by ω_x^+

contributing to the formation of the slipstream velocity. However, in the cases with vortex generators, the streamwise vortex pair formed from separation from the roof of the train tail shows a delayed interaction with the pair that from close to the ground, resulting in the attenuation of the main trailing vortex pair. Moreover, extra vortex structures associated with the VGs generators, as shown in the figure, feed in additional vorticity near the train tail tip counteracting the adverse pressure gradient in the original case.

To further highlight the formation and advection of the wake flow vorticity, Figure 18 illustrates the boundary of the trailing-vortex structure on three cross-stream planes between x=0.1H and 5H through an iso-line of Γ_2=2/π. The latter has been used extensively to delineate the extent of a vortex-dominated region [27, 46], especially for examining experimental velocity fields. The trackside and platform slipstream measurement locations are also indicated in Figure 18. As shown in this figure, the pair of trailing vortices is split into two segments by the VGs on the plane x=0.1H for both cases with vortex generators. As the flow moves downstream, the trailing vortices exhibit a rolling motion over the rail, becoming progressively wider while the magnitude of vorticity decreases. To quantitatively analyze the vorticity variations on different planes in the wake region, the circulation is calculated and presented in Table 4, over an integration area denoted by S as shown in Figure 18. The circulation is defined as follows:

$$\gamma = \iint_S \omega_x^+ \mathrm{d}S \tag{6}$$

On the plane at x=5H, which is close to the location of the peak slipstream values, the circulations in cases VG_A and VG_{AB} are reduced by 15.9% and 23.2%, respectively, relative to the original case, which is comparable to the decrease observed in the slipstream values. The lower circulation in each leg additionally means that there is less outwards advection caused by the image vortex system. Also note that this figure shows that the spanwise vortex maxima, which are associated with strong axial flow and therefore high slipstream velocities, are situated slightly closer to y/H=0 in both vortex generator cases.

Figures 19 to 21 illustrate the flow on the upper surface of the tail car including the vortex structures, the downwash flow, and the boundary layer. These figures provide a detailed depiction of how the vortex generators influence the flow relative to the original case, revealing the underlying reasons for the reduction in peak slipstream values and turbulent kinetic energy in the wake region. The four selected planes in the figures sequentially represent the vortex structures at the locations of the two pairs of vortex generators, as well as the upstream and downstream around the nose tip. From the vortex structures shown in Figure 19, it can be observed that the vortex generator at position A generates a strong vortex, V_{1A}, with an opposite direction to the longitudinal vortex V_t. The interaction between V_{1A} and V_t elevates the vortex core position of V_t, resulting in a more concentrated vorticity on the plane x=−0.11H. The interaction between these two pairs of longitudinal vortices persists and develops

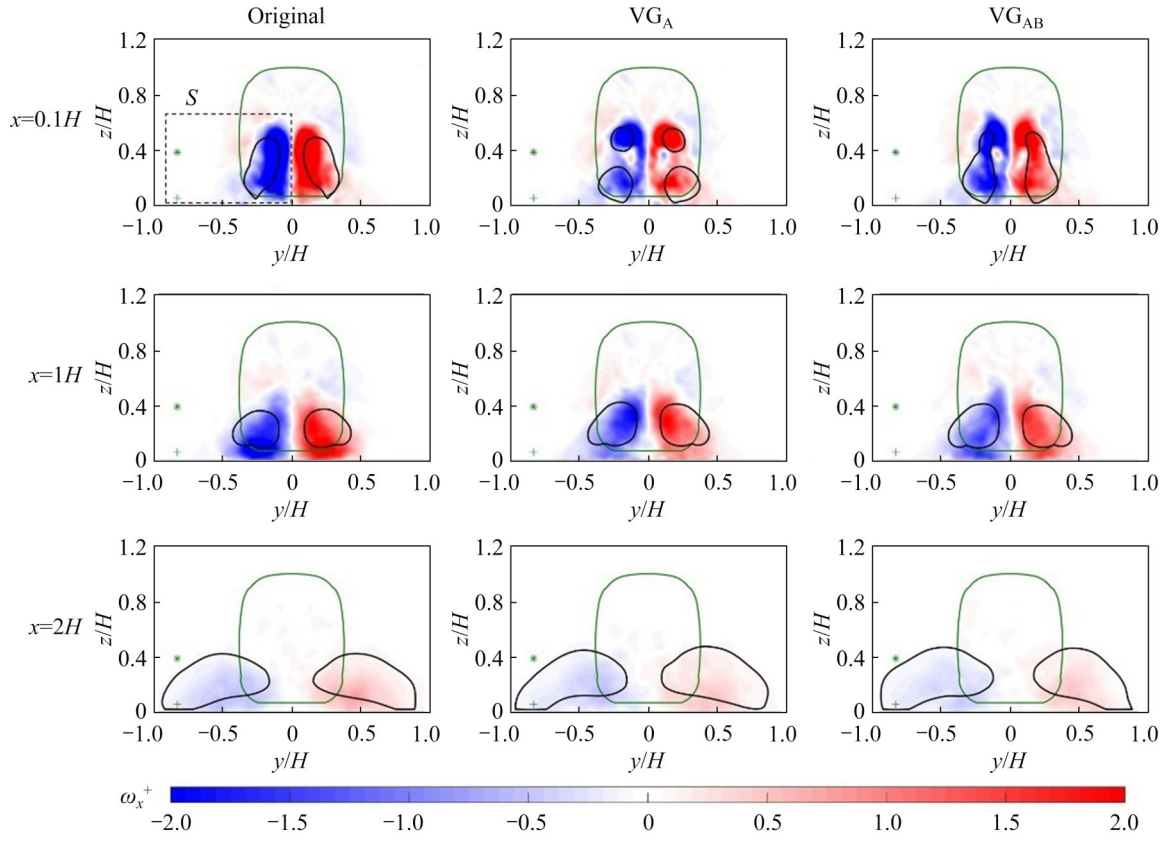


Figure 18 The comparison of the wake development downstream depicted by streamwise vorticity color contours, and isolines of $\Gamma_2=2/\pi$ depicting the vortex core regions

Table 4 The total vortex circulation in the left leg of the trailing vortex pair on different planes in the train wake

Case	$x=0.1H$	$x=1H$	$x=5H$
Original	0.288	0.190	0.082
VG_A	0.195	0.155	0.069
VG_{AB}	0.207	0.156	0.063

downstream to the plane $x=-0.03H$, where V_{2A} is formed, further intensifying the interaction. When the longitudinal vortex V_t detaches from the tip tail of the train, it rapidly rolls up the surrounding airflow, significantly increasing the extent of the vortex-dominated region as shown on the plane $x=0.05H$. However, the VGs prevent this process by generating a counter-rotating motion relative to the longitudinal vortex of the train, resulting in a notable reduction in vorticity on this plane, as previously shown in Table 4.

When vortex generators are placed at both locations A and B, the vortex V_{1B} formed at location B interacts earlier with the train's longitudinal vortex, thereby weakening its intensity. The difference is demonstrated on the planes at $x=-0.11H$ and $x=0.05H$, where the intensities of both V_t and V_{1A} are noticeably reduced in the case VG_{AB} relative to the case VG_A. Figure 20 illustrates the impact of vortex generators on the downwash flow through the contours of the vertical velocity component on the planes from $x=-0.28H$ to $x=0.05H$. Here, the velocity components are normalized by the freestream velocity U_∞. It reveals that the vortex generator significantly weakens the intensity of the downwash flow, which is a primary reason for the changes in the vortex structures beneath the nose tip of the train. Figure 21 shows the influence of the vortex generator on the boundary layer of the train depicted by streamwise velocity color contours, with two pink contour lines representing $0.99U$ and $0.4U$, respectively. It is evident that the vortex generators decelerate the airflow around the VGs, which in turn increases the positive pressure on the upper surface of the tail car, as demonstrated in Figure 22. Following the formulation widely used in aerodynamics [47, 48],

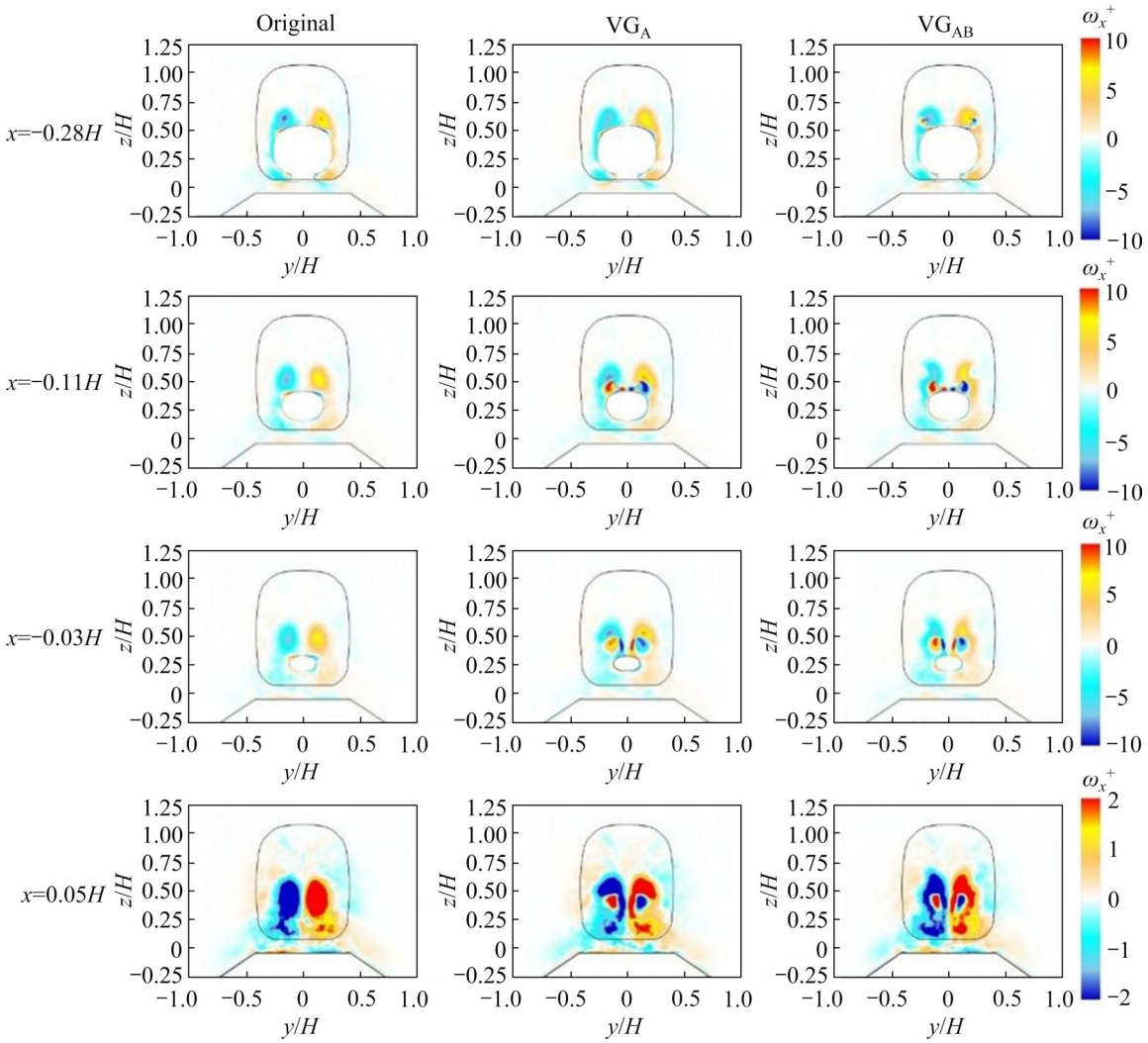


Figure 19 Comparison of the vortex structures around the nose tip through streamwise vorticity color contours on the planes from x=−0.28H to x=0.05H(Note that the color scale is varied to best highlight the vortex structures)

the pressure coefficient is defined as:

$$C_{\mathrm{p}}=\frac{p-p_{\mathrm{ref}}}{0.5\rho U_{\infty}^{2}} \tag{7}$$

where ρ and U_{∞} signify the air density and the speed of the train, respectively; p is the measured pressure on the train surface, and p_{ref} is the reference pressure.

In summary, this study advances the fundamental understanding of vortex generator (VG) applications in high-speed train aerodynamics by elucidating an innovative flow control mechanism. The results demonstrate that VGs installed near the tail car nose tip generate opposite sign vortices that strategically interact with and attenuate the natural trailing vortices. This vortex interference mechanism effectively reduces both the mean slipstream velocity and turbulent fluctuations in the wake region. Based on the fundamental flow control mechanism revealed in this study, VGs installed in a similar configuration should maintain a comparable weakening effect on slipstream across different operational speeds and for trains with analogous geometries. However, their performance under more complex conditions involving crosswinds remains to be explored. Such investigations will be undertaken in the future to better assess the practical applicability of VGs.

4 Conclusions

The IDDES method was employed to investigate the impact of vortex generators on the wake flow dynamics of high-speed trains. The comparison was given through slipstream velocity, turbulent kinetic energy and flow structures for

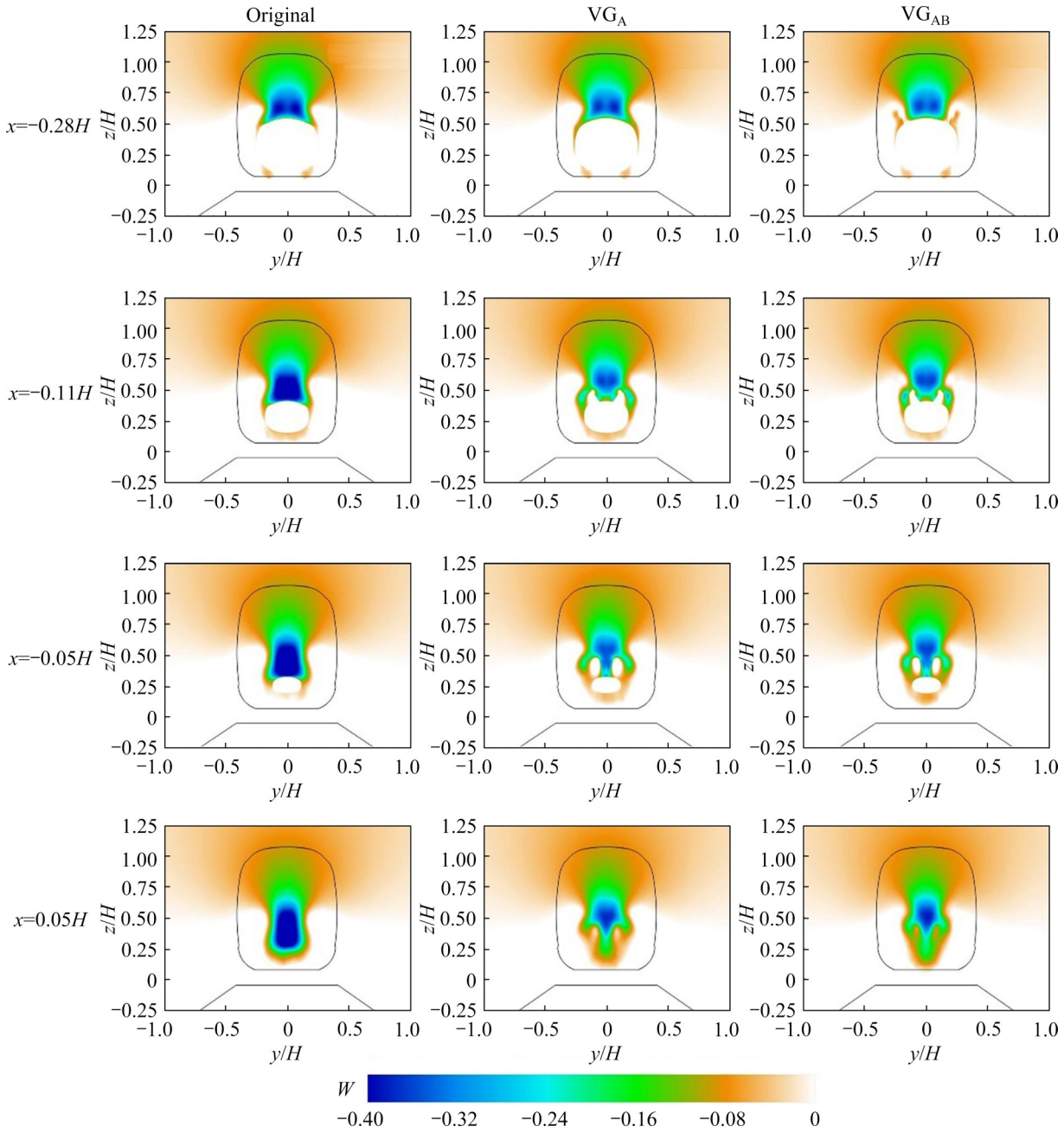


Figure 20 Comparison of the downwash flow around the nose tip through normalized vertical velocity color contours on the planes from x=−0.28H to x=0.05H

different implementations of VGs. Numerical predictions indicate that strategic placement of VGs reduces the peak values of the slipstream velocity and turbulent kinetic energy in the wake through the generation of additional locally opposite-signed vorticity, which cross-annihilates and cross-diffuses with the vorticity of the forming and advecting trailing vortex pair. The principal conclusions drawn from this research are outlined as follows:

1) The installation of a single pair of vortex generators near the train tail tip resulted in an approximately 15% reduction in the upper limit of slipstream velocity relative to the original case. Subsequently, an additional pair of vortex generators located upstream caused further decreases of 18% in the average and 16% in the standard deviation, resulting in a 17% reduction in the upper limit. These reductions in slipstream values were attributed to the reduction in the vortex intensity of the trailing pair induced by the vortex generators.

2) The turbulent kinetic energy was diminished

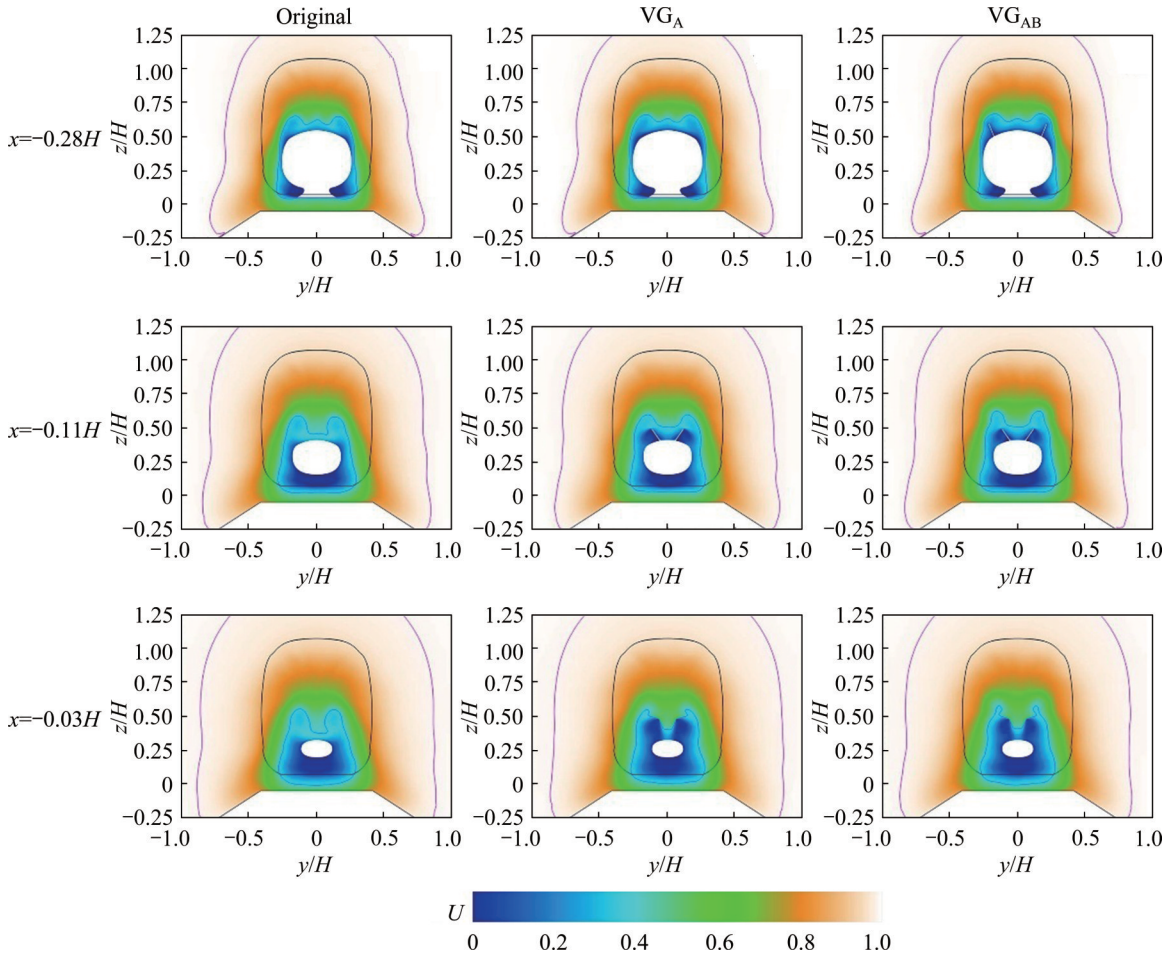


Figure 21 Comparison of the boundary layer depicted by streamwise velocity color contours and isolines of 0.4U and 0.99U

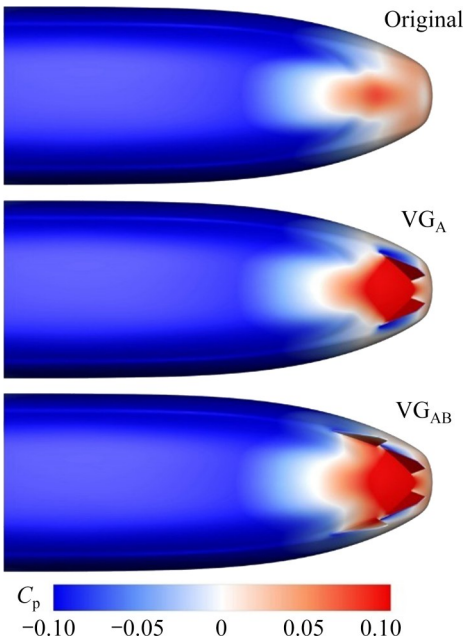


Figure 22 Pressure coefficient on the upper of surface of the tail section showing a comparison of the influence of placing vortex generators as positions A (middle) and AB (bottom) against the base case (top)

in the wake region of the train as the vortex generators decelerated the downwash flow and fed in additional opposing vorticity. The net effect was to reduce the kinetic energy production term as the longitudinal vortex pair advected downstream.

3) Indeed, the primary alteration to the vortical wake structure induced by the vortex generators is the formation of an additional streamwise opposing vortex pair. This vorticity raises the core position of the train's longitudinal vortex, leading to more concentrated vorticity on the upper surface of the tail car. As the flow moves downwards, the sustained interaction between these two counter-rotating vortices, through cross-annihilation and cross-diffusion, results in a reduction of both turbulent kinetic energy and slipstream. The weakened resultant trailing vortex also results in lower outwards velocity from advection produced by its image pair below the ground. Given that the pair is also associated with faster moving

streamwise velocity (in the stationary atmosphere reference frame), reducing its outward motion is favorable for slipstream reduction.

4) Unlike conventional vortex generators designed to weaken primary separation vortices, this study demonstrates that strategically positioned VGs can generate counter-rotating vortices that effectively interact with natural trailing vortices. Future studies should focus on the systematic optimization of vortex generator configurations to maximise aerodynamic performance under complex operational conditions. Furthermore, comprehensive experimental validation is essential to verify the effectiveness and practical applicability of the optimized VG designs.

Acknowledgement

The authors acknowledge the computing resources provided by the High-speed Train Research Center and the High Performance Computing Center of Central South University, China.

Contributors

The overarching research goals were developed by HAN Shuai, ZHANG Jie, and THOMPSON Mark. HAN Shuai and TUDBALL-SMITH Daniel constructed the CFD computational model and performed data post-processing. HAN Shuai and BURTON David analyzed the calculated results. The initial draft of the manuscript was written by HAN Shuai, ZHANG Jie, and THOMPSON Mark. All authors replied to reviewers' comments and revised the final version.

Conflict of interest

The authors have no conflicts to disclose.

References

[1] GAO Hong-rui, LIU Tang-hong, CHEN Xiao-dong, et al. Aerodynamic and dynamic behaviour of a train in cutting-viaduct-cutting sections with windbreaks in complex terrains under crosswinds: Key factors [J]. Engineering Structures, 2025, 328: 119728. DOI:10.1016/j.engstruct.2025.119728.

[2] ZHANG Jie, ZHANG Mo-lin, HAN Shuai, et al. A novel asymptotic linear method for micro-pressure wave mitigation at high-speed maglev tunnel exit: A case study with various open ratios on tunnel hoods [J]. Journal of Central South University, 2025, 32(5): 1955－1972. DOI: 10.1007/s11771-025-5900-z.

[3] CHEN Jia-zheng, XU Ao, LIU Tang-hong, et al. On enhancing anti-overturning performance of a high-speed train with side airfoils in crosswinds [J]. Journal of Wind Engineering and Industrial Aerodynamics, 2025, 264: 106151. DOI:10.1016/j.jweia.2025.106151.

[4] BAKER C J, DALLEY S J, JOHNSON T, et al. The slipstream and wake of a high-speed train [J]. Proceedings of the Institution of Mechanical Engineers, Part F: Journal of Rail and Rapid Transit, 2001, 215(2): 83－99. DOI: 10.1243/0954409011531422.

[5] HUANG Feng-yi, XU Ao, ZHANG Jie, et al. A passive flow control method with winglets installed on leeward side of a high-speed train for improvement of anti-overturning performance under crosswinds [J]. Physics of Fluids, 2025, 37(3): 035180. DOI:10.1063/5.0258249.

[6] ZHANG Jie, XU Ao, HUANG Feng-yi, et al. A novel vortex control method for improving anti-overturning performance of a high-speed train with leeward airbag structures under crosswinds [J]. Physics of Fluids, 2024, 36(6): 065146. DOI: 10.1063/5.0211370.

[7] HAN Shuai, ZHANG Jie, XIONG Xiao-hui, et al. Influence of high-speed maglev train speed on tunnel aerodynamic effects [J]. Building and Environment, 2022, 223: 109460. DOI:10.1016/j.buildenv.2022.109460.

[8] GAO Guang-jun, XIANG Nan-shen, DING Yan-si, et al. A smooth-guiding method for aerodynamic drag reduction on key regions of a high-speed train [J]. Mechanics Based Design of Structures and Machines, 2025: 1 － 25. DOI: 10.1080/15397734.2025.2537310.

[9] JIANG Chen, LONG Jin-lan, LI Yan-song, et al. Numerical investigation on the aerodynamic drag reduction based on bottom deflectors and streamlined bogies of a high-speed train [J]. Journal of Central South University, 2024, 31(9): 3312−3328. DOI:10.1007/s11771-024-5763-8.

[10] MOREL T. Effect of base slant on flow in the near wake of an axisymmetric cylinder [J]. Aeronautical Quarterly, 1980, 31(2): 132−147. DOI:10.1017/s0001925900010957.

[11] MULD T W, EFRAIMSSON G, HENNINGSON D S. Flow structures around a high-speed train extracted using proper orthogonal decomposition and dynamic mode decomposition [J]. Computers & Fluids, 2012, 57: 87－97. DOI: 10.1016/j.compfluid.2011.12.012.

[12] BELL J R, BURTON D, THOMPSON M, et al. Wind tunnel analysis of the slipstream and wake of a high-speed train [J]. Journal of Wind Engineering and Industrial Aerodynamics, 2014, 134: 122−138. DOI:10.1016/j.jweia.2014.09.004.

[13] WANG Xin-ran, LIU Tang-hong, XIA Yu-tao, et al. Effect of railway cutting depths on running safety and pantograph－catenary interaction of trains under crosswind [J]. Journal of Wind Engineering and Industrial Aerodynamics, 2024, 245: 105659. DOI:10.1016/j.jweia.2024.105659.

[14] BAKER C. The flow around high speed trains [J]. Journal of Wind Engineering and Industrial Aerodynamics, 2010, 98(6, 7): 277−298. DOI:10.1016/j.jweia.2009.11.002.

[15] LIN J C. Review of research on low-profile vortex generators to control boundary-layer separation [J]. Progress in Aerospace Sciences, 2002, 38(4, 5): 389−420. DOI: 10.1016/

S0376-0421(02)00010-6.

[16] KATZ J. Aerodynamics of race cars [J]. Annual Review of Fluid Mechanics, 2006, 38: 27 − 63. DOI: 10.1146/annurev.fluid.38.050304.092016.

[17] GIBERTINI G, BONIFACE J C, ZANOTTI A, et al. Helicopter drag reduction by vortex generators [J]. Aerospace Science and Technology, 2015, 47: 324−339. DOI: 10.1016/j.ast.2015.10.004.

[18] MEREU R, PASSONI S, INZOLI F. Scale-resolving CFD modeling of a thick wind turbine airfoil with application of vortex generators: Validation and sensitivity analyses [J]. Energy, 2019, 187: 115969. DOI: 10.1016/j. energy. 2019.115969.

[19] MANOLESOS M, CHNG L, KAUFMANN N, et al. Using vortex generators for flow separation control on tidal turbine profiles and blades [J]. Renewable Energy, 2023, 205: 1025−1039. DOI:10.1016/j.renene.2023.02.009.

[20] KERHO M, HUTCHERSON S, BLACKWELDER R F, et al. Vortex generators used to control laminar separation bubbles [J]. Journal of Aircraft, 1993, 30(3): 315−319. DOI: 10.2514/3.46336.

[21] KATZ J, MOREY F. Aerodynamics of large-scale vortex generator in ground effect [J]. Journal of Fluids Engineering, 2008, 130(7): 071101. DOI:10.1115/1.2948361.

[22] WANG Shi-bo, BURTON D, HERBST A H, et al. The effect of the ground condition on high-speed train slipstream [J]. Journal of Wind Engineering and Industrial Aerodynamics, 2018, 172: 230−243. DOI:10.1016/j.jweia.2017.11.009.

[23] KRAJNOVIĆ S. Shape optimization of high-speed trains for improved aerodynamic performance [J]. Proceedings of the Institution of Mechanical Engineers, Part F: Journal of Rail and Rapid Transit, 2009, 223(5): 439 − 452. DOI: 10.1243/09544097jrrt251.

[24] LI Tian, LIANG Hao, ZHANG Jie, et al. Numerical study on aerodynamic resistance reduction of high-speed train using vortex generator [J]. Engineering Applications of Computational Fluid Mechanics, 2023, 17: e2153925. DOI: 10.1080/19942060.2022.2153925.

[25] ZHANG Jie, HUANG Feng-yi, YU Yi-zheng, et al. A novel wake flow control method for drag reduction of a high-speed train with vortex generators installing on streamlined tail nose [J]. Physics of Fluids, 2023, 35(10): 105139. DOI: 10.1063/5.0173350.

[26] Standards Committee Railway. Normenausshuss Fahrweg and Schienenfahrzenge (FSF): DIN EN14067-4 [S]. 2014.

[27] WANG Shi-bo, BURTON D, HERBST A, et al. The effect of bogies on high-speed train slipstream and wake [J]. Journal of Fluids and Structures, 2018, 83: 471−489. DOI:10.1016/j.jfluidstructs.2018.03.013.

[28] HE Kan, SU Xin-chao, GAO Guang-jun, et al. Evaluation of LES, IDDES and URANS for prediction of flow around a streamlined high-speed train [J]. Journal of Wind Engineering and Industrial Aerodynamics, 2022, 223: 104952. DOI:10.1016/j.jweia.2022.104952.

[29] BELL J R, BURTON D, THOMPSON M C, et al. A wind-tunnel methodology for assessing the slipstream of high-speed trains [J]. Journal of Wind Engineering and Industrial Aerodynamics, 2017, 166: 1−19. DOI:10.1016/j.jweia.2017.03.012.

[30] WANG Dong-wei, CHEN Chun-jun, HU Jia, et al. The effect of Reynolds number on the unsteady wake of a high-speed train [J]. Journal of Wind Engineering and Industrial Aerodynamics, 2020, 204: 104223. DOI: 10.1016/j. jweia.2020.104223.

[31] HAN Shuai, WANG Yi-han, ZHANG Mo-lin, et al. An adaptive drag reduction method for high-speed trains across variable Reynolds numbers [J]. Physics of Fluids, 2025, 37(8): 085208. DOI:10.1063/5.0281229.

[32] HUANG Feng-yi, SHANG Wen-fei, ZHANG Jie, et al. Optimization of crosswind stability for high-speed trains: Aerodynamic analysis of leeward winglet deflection angles [J]. Journal of Central South University, 2025, 32(12): 5124−5142. DOI:10.1007/s11771-025-6036-x.

[33] ZHANG Jie, DING Yan-si, WANG Yi-han, et al. A novel bionic Coleoptera pantograph deflector for aerodynamic drag reduction of a high-speed train [J]. Journal of Central South University, 2023, 30(6): 2064 − 2080. DOI: 10.1007/s11771-023-5349-x.

[34] ADAMU A, ZHANG Jie, TAJUDEEN H. Aerodynamic drag reduction of a high-speed train with cavities on bogie regions [J]. Physics of Fluids, 2025, 37(6): 065143. DOI: 10.1063/5.0271382.

[35] SPALART P R. Detached-eddy simulation [J]. Annual Review of Fluid Mechanics, 2009, 41: 181 − 202. DOI: 10.1146/annurev.fluid.010908.165130.

[36] ZHANG Jie, WANG Fan, HAN Shuai, et al. An investigation on the switching of asymmetric wake flow and the bi-stable flow states of a simplified heavy vehicle [J]. Engineering Applications of Computational Fluid Mechanics, 2022, 16(1): 2035−2055. DOI:10.1080/19942060.2022.2130432.

[37] ZENG Hao-yang, LIU Tang-hong, CHEN Xiao-dong, et al. Study on the influence of asymmetric mountain structures at tunnel portals on the aerodynamics of intersecting trains [J]. Transportation Safety and Environment, 2025, 7: tdaf016. DOI:10.1093/tse/tdaf016.

[38] ZHANG Jie, WANG Yi-han, WANG Yu-ge, et al. Pressure wave characteristics in high-speed maglev tunnels with various arch lattice-shell lengths inside hoods [J]. Physics of Fluids, 2025, 37(2): 026125. DOI:10.1063/5.0255132.

[39] WANG Shi-bo, BELL J R, BURTON D, et al. The performance of different turbulence models (URANS, SAS and DES) for predicting high-speed train slipstream [J]. Journal of Wind Engineering and Industrial Aerodynamics, 2017, 165: 46−57. DOI:10.1016/j.jweia.2017.03.001.

[40] HAN Shuai, XIANG Nan-shen, HUANG Feng-yi, et al. On reducing high-speed train slipstream using vortex generators [J]. Physics of Fluids, 2025, 37(5): 055115. DOI: 10.1063/5.0270021.

[41] BELL J R, BURTON D, THOMPSON M C, et al. Moving model analysis of the slipstream and wake of a high-speed train [J]. Journal of Wind Engineering and Industrial Aerodynamics, 2015, 136: 127 − 137. DOI: 10.1016/j. jweia.2014.09.007.

[42] XIA Chao, WANG Han-feng, SHAN Xi-zhuang, et al. Effects of ground configurations on the slipstream and near wake of a high-speed train [J]. Journal of Wind Engineering and Industrial Aerodynamics, 2017, 168: 177 − 189. DOI: 10.1016/j.jweia.2017.06.005.

[43] European Union Agency for Railways. Commission regulation (EU) No. 1302/2014: Concerning a technical specification for interoperability relating to the “rolling stock-locomotives and passenger rolling stock” subsystem of the rail system [R]. 2014.

[44] CHEN Guang, LI Xiao-bai, LIU Zhen, et al. Dynamic analysis of the effect of nose length on train aerodynamic performance [J]. Journal of Wind Engineering and Industrial Aerodynamics, 2019, 184: 198–208. DOI: 10.1016/j. jweia. 2018.11.021.

[45] ZHANG Jie, HAN Shuai, JI Peng, et al. Windproof performance improvement of windbreak walls on the transition connecting a realistic embankment and a hill cut along the high-speed railway [J]. Mechanics Based Design of Structures and Machines, 2025: 1–22. DOI: 10.1080/15397734.2025.2510583.

[46] GRAFTIEAUX L, MICHARD M, GROSJEAN N. Combining PIV, POD and vortex identification algorithms for the study of unsteady turbulent swirling flows [J]. Measurement Science and Technology, 2001, 12(9): 1422–1429. DOI:10.1088/0957-0233/12/9/307.

[47] WANG Y, YU Y, HAN S, et al. A novel arch lattice-shell tunnel hood design for mitigating pressure wave characteristics during a high-speed maglev train passage through a tunnel at various train speeds [J]. Tunnelling and Underground Space Technology, 2026, 168: 107015. DOI: 10.1016/j.tust.2026.107015.

[48] ZHANG J, MELAKU T G, ADAMU A, et al. Impact of incoming flow on wake asymmetry of a simplified vehicle: The Reynolds number effect [J]. Journal of Wind Engineering and Industrial Aerodynamics, 2026, 268: 106291. DOI:10.1016/j.jweia.2026.106291.

(Edited by ZHENG Yu-tong)

中文导读

采用涡发生器抑制高速列车尾流特性的新型被动流动控制方法：机理与应用

摘要：本文提出了一种在高速列车尾部加装涡发生器(VGs)以降低高速列车尾迹区列车风峰值和湍动能的被动流动控制方法。采用改进延迟分离涡模拟(IDDES)研究了涡发生器对列车尾迹流动的影响，并通过已有试验数据及文献中数值仿真算例验证了数值仿真方法。研究结果表明，合理布置涡发生器可分别降低列车风平均值($U_{slipstream}$)、正峰值($U_{slipstream,\ max}$)约17%和15%，同时延迟列车风峰值出现位置(约一倍列车高度)，降低了列车风对站台候车乘客及轨道旁作业人员的危害。安装涡发生器后，列车尾部下洗流减弱，并削弱了列车尾流中的剪切项，有效降低了列车尾迹区湍动能。涡发生器产生的与列车尾涡旋向相反的涡对结构改变了列车非定常尾涡结构，二者形成抵消作用，降低了列车尾涡强度，从而减缓了列车风峰值。该被动流动控制方法将为高速列车尾涡调控提供一种全新的、有效的解决方案。

关键词：高速列车；涡发生器；列车风；尾迹；被动流动控制